Cloud Thermodynamic-Phase Determination From Near-Infrared Spectra of Reflected Sunlight

WOUTER H. KNAP, PIET STAMMES, AND ROBERT B. A. KOELEMEIJER

Royal Netherlands Meteorological Institute, De Bilt, Netherlands

(Manuscript received 29 March 2001, in final form 22 June 2001)

ABSTRACT

A simple method for the determination of the thermodynamic phase of clouds over ocean from near-infrared spectra of reflected sunlight is presented. The method is based on thresholding the parameter $S_{1.67}$ (in percent), which is defined as the ratio of the difference between the spectral reflectivities at 1.70 and 1.64 μm to the reflectivity at 1.64 μm. Radiative transfer calculations for different cloudy atmospheres over ocean are presented to show that $S_{1.67} \approx 0$ for water clouds and $S_{1.67} > 0$ for ice clouds and mixed-phase clouds. It is shown that $S_{1.67}$ is sensitive to the presence of ice particles in clouds, and depends primarily on ice-cloud optical thickness and crystal size. The method is relatively independent of viewing and solar geometry because it is based on spectral absorption properties rather than scattering properties of clouds.

The method is thoroughly analyzed using near-infrared reflectivity spectra made by the Airborne Visible and Infrared Imaging Spectrometer (AVIRIS) over a well-defined cloud system of stratocumulus and cirrus situated over the Pacific Ocean. The location of water and ice clouds, derived from pilot information and from visual interpretation of the 0.87-μm (atmospheric window) and 1.38-μm (water vapor absorption band) images, is well reproduced by thresholding $S_{1.67}$ according to the following scheme: $S_{1.67} \leq 2\%$, water cloud; $2\% < S_{1.67} < 10\%$, optically thin ice cloud; and $S_{1.67} \geq 10\%$, optically thick ice cloud.

On the basis of radiative transfer calculations it is shown that the method may lead to misclassifications in cases where optically thin clouds are present over snow. It is suggested that this also applies to minerals, rocks, and (dry) soils. On the other hand, it is shown that there is no fundamental difference between $S_{1.67}$ cloud-phase determination over ocean and green vegetation. It is therefore expected that the method is suitable for application to measurements made over large parts of the globe by spaceborne spectrometers, which are able to identify the shape of the reflectivity spectrum around 1.67 μm, such as the Scanning Imaging Absorption Spectrometer for Atmospheric Chartography (SCIAMACHY), which is scheduled for launch on the European Space Agency's (ESA) Environmental Satellite (ENVISAT) in 2002.

1. Introduction

Clouds have a great influence on the radiation balance of the earth's surface and atmosphere because they reflect and absorb solar radiation and emit and absorb terrestrial radiation. The interaction between clouds and radiation determines to a large extent the energy balance at any level in the atmosphere and is therefore very important for the surface and atmospheric temperatures. This, in turn, implies the crucial role clouds play in the earth's climate (Stephens et al. 1990; Hartmann 1993). The radiative effects of clouds depend critically on cloud properties such as height, optical thickness, thermodynamic phase (i.e., liquid water or ice), and particle size. Although in recent years the representation of clouds in climate models has been greatly improved, there is still significant uncertainty in climate change simulations. Much of this uncertainty is caused by cloud-radiative feedback processes that have largely unknown sign and amplitude (Stocker et al. 2001). Satellite instruments provide measurements on a global scale needed for model validation and improvement of the understanding of the role of clouds in the earth's climate, both presently and in the future. The present paper deals with one aspect of these measurements, namely, the determination of the cloud thermodynamic phase.

The accuracy of satellite retrievals of cloud optical thickness and particle size depends crucially on the assumed particle shape in radiative transfer models. Since the shape and therefore the single scattering properties of water droplets and ice crystals are very different (see e.g., Mishchenko et al. 1996; Doutriaux-Boucher et al. 2000), it is essential to know if one is dealing with water clouds or ice clouds, prior to retrieving other cloud properties. In fact, the determination of the thermodynamic phase (or simply, the phase) of clouds should be regarded as the first step in algorithms designed for the retrieval of cloud properties from satellite measurements.

Corresponding author address: Dr. W. H. Knap, Royal Netherlands Meteorological Institute (KNMI), P.O. Box 21, 3730 AE De Bilt, Netherlands.
E-mail: knap@knmi.nl

Several methods of determining the cloud phase from satellite measurements exist. The best-known method is based on thresholding the cloud-top temperature derived from thermal infrared radiances (Rossow and Schiffer 1999). Key and Intrieri (2000) describe cloud-phase determination using the Advanced Very High Resolution Radiometer–reflected infrared (3.7 μm) and thermal (11 and 12 μm) channels. Baum et al. (2000) improved a trispectral thermal infrared method for Moderate-Resolution Imaging Spectroradiometer by utilizing visible (0.65 μm) and near-infrared (1.63 and 1.90 μm) reflectivities. Another method that addresses cirrus cloud detection only, is based on radiance measurements made in the 1.38-μm water vapor absorption band. The idea behind this method is that, because of strong absorption of scattered solar radiation by water vapor in the lower troposphere, radiances measured at this wavelength almost exclusively result from scattering of solar radiation by cirrus clouds (Gao et al. 1993). A third method is based on the fact that polarized radiances are particularly sensitive to the cloud particle shape. Riedi et al. (2000) describe how they used the angular distribution of polarized radiation to discriminate between water and ice clouds.

Pilewskie and Twomey (1987a,b) demonstrated the possibility of determining the cloud phase using cloud reflectivity or transmissivity measurements in the wavelength region between 1.55 and 1.75 μm. The authors suggest that differences between water cloud and ice cloud reflectivity spectra (found in ground-based measurements of cloud sides) are related to differences in the absorption spectra of water and ice. In the present paper, this idea is further developed by means of detailed radiative transfer calculations in the range 1.4–1.9 μm for atmospheres containing clouds over ocean, green vegetation, or snow. The calculations for clouds over ocean show that top-of-atmosphere near-infrared reflectivity spectra around 1.67 μm of water and ice clouds are clearly different with respect to their shape. This shape difference is exploited to formulate a simple cloud-phase determination algorithm for clouds over ocean. The algorithm is evaluated using Airborne Visible Infrared Imaging Spectrometer (AVIRIS) spectra made over a well-defined cloud system of marine stratocumulus (water cloud) and cirrus (ice cloud). Both of these cloud types are spatially and temporally persistent in the earth's atmosphere (King 1993), so the case presented here is useful in the light of global cloud-phase retrieval.

The motivation behind the development of the cloud phase algorithm presented here is found in the fact that global measurements of the earth in the near-infrared will be made by the Scanning Imaging Absorption Spectrometer for Atmospheric Chartography (SCIAMACHY) (Bovensmann et al. 1999). This instrument will be flown on the European Space Agency's (ESA) Environmental Satellite (ENVISAT), which is scheduled for launch in 2002. SCIAMACHY has been designed for measuring radiances in the ultraviolet, visible, and near-infrared wavelength regions (0.240–2.380 μm) at relatively high spectral resolution (0.2–1.5 nm). The mission objectives of SCIAMACHY are mainly defined in the area of atmospheric chemistry, but also clouds and aerosols are to be studied using SCIAMACHY's spectrometric characteristics. The spectral range of 1.60–1.75 μm has specifically been added to the instrument for cloud-phase determination.

The organization of this paper is as follows. First, the fundamentals of the method are presented, together with radiative transfer calculations for one- and two-layered water and ice clouds over ocean (sections 2a–e). In sections 2f and 2g calculations for mixed-phase clouds and clouds over different land surfaces are shown. In section 2h, the cloud-phase determination algorithm for clouds over ocean is presented. Section 3 begins with some general information about AVIRIS (section 3a) and the cloudy scene that has been selected for analysis (section 3b). In section 3c, AVIRIS spectra made over water clouds, ice clouds, and a clear ocean area are presented and discussed in the light of the radiative transfer calculations. The shape of different cloudy AVIRIS spectra is quantified and analyzed in section 3d. Classification according to the cloud phase is performed in section 3e. Conclusions are drawn in section 4.

2. Method of cloud-phase determination

a. Principle

The starting point of our method of determination of the thermodynamic phase of clouds is the spectral shape difference in the absorption spectra of pure water and ice at the wavelength $\lambda = 1.67$ μm. At this wavelength the spectral slope in the imaginary part of the refractive index is about zero for water but negative for ice (Fig. 1; arrows). Since absorption by both water and ice is relatively strong in the near-infrared, it is expected that the 1.67 μm absorption structure seen in Fig. 1 shows up in the top-of-atmosphere (TOA) spectral reflectivity R_λ of water and ice clouds, which is defined as follows:

$$R_\lambda = \frac{\pi L_\lambda}{S_{o,\lambda} \cos\theta_o}, \tag{1}$$

where L_λ is the reflected spectral radiance (W m^{-2} sr^{-1} nm^{-1}) for the cloud–atmosphere system, $S_{o,\lambda}$ is the TOA spectral solar irradiance (W m^{-2} nm^{-1}), and θ_o is the solar zenith angle. Speaking in qualitative terms, the principle of the method for the determination of the thermodynamic phase of clouds is based on exploiting the spectral shape difference in R_λ at 1.67 μm for water and ice clouds. In sections 2b,c, the principle will be given a quantitative basis by means of radiative transfer calculations for atmospheres containing water or ice clouds.

The absorption structure in R_λ can only be detected by a satellite instrument if the radiance originating from

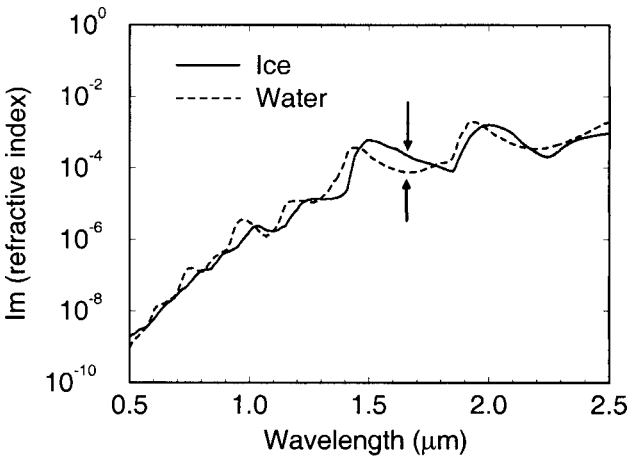

FIG. 1. Imaginary part of the refractive index of ice and water as a function of wavelength between 0.5 and 2.5 μm. The arrows indicate the 1.67-μm wavelength where the spectral slopes for water and ice are highly different. Data sources: Hale and Querry (1973), Palmer and Williams (1974), and Downing and Williams (1975) for water; and Warren (1984) for ice.

the cloud is not too much affected by gaseous absorption in the atmosphere between the cloud and the satellite instrument. Although some absorption by CO_2 is present (see section 3a), this condition is largely fulfilled at wavelengths near 1.67 μm, where the atmosphere is highly transparant for water vapor. Because the 1.67-μm wavelength is situated in an atmospheric window, the principle described above allows one to directly exploit the differing absorption properties of water and ice for cloud-phase determination, without being dependent on factors such as atmospheric composition and cloud height.

b. Radiative transfer model for cloudy atmospheres

In order to quantitatively investigate the use of the 1.67-μm absorption structure in R_λ for cloud-phase determination, calculations for multiple scattering of sunlight in a cloudy atmosphere over ocean were performed with the Doubling-Adding Royal Netherlands Meteorological Institute radiative transfer model (Stammes 1994). In this model, multiple scattering is calculated by means of the doubling-adding method according to de Haan et al. (1987). The model atmosphere consists of plane-parallel Rayleigh-scattering layers over a Lambertian surface. Cloud particles can be mixed in any of these layers. For the calculations presented here, the model atmosphere contains neither aerosols nor absorbing gases. Standard midlatitude summer profiles for temperature and pressure were taken from Anderson et al. (1986). In order to present calculations for water and ice clouds, two standard cloudy model atmospheres are defined: one containing a water cloud and the other containing an ice cloud. The governing characteristics of the cloudy atmospheres are listed in Table 1, together with information about the surface and the solar and viewing geometries used. The standard water cloud consists of spherical water droplets of which the single scattering properties were calculated on the basis of Mie theory (de Rooij and Van der Stap 1984). The effective radius of the water droplets is 10 μm, which is a typical value for marine stratocumulus. The standard ice cloud consists of so-called imperfect hexagonal ice crystals (Hess et al. 1998). These crystals have the basic hexagonal shape (either columnar or plate-like) with a certain degree of small-scale roughness on their surface. With respect to single scattering properties, the imperfect crystal [like, e.g., the inhomogeneous hexagonal monocrystal (C.-Labonnote et al. 2001)] bridges the gap between the perfect hexagonal crystal and complex-shaped models for natural ice crystals, such as disordered fractals (Macke et al. 1996). The imperfect ice crystal model has been successfully used to explain reflectivities of cirrus as measured by the second Along-Track Scanning Radiometer (ATSR-2, a spaceborne radiometer) and we believe it to be suitable for the representation of the single scattering properties of ice clouds. For the ice crystal size and shape, crystal type C2 of the Cirrus Optical Properties (COP) data library was used (Hess and Wiegner 1994; and Table 1). Compared to the other crystals in this library, C2 has an intermediate size. In real cirrus clouds, both smaller and larger crystals of different shapes can be found. Therefore, we feel that crystal C2 provides a workable starting point for the standard calculations presented in this paper. For detailed information about the single scattering properties (such as the phase function) of imperfect hexagonal ice crystals and about the application to ATSR-2 measurements the reader is referred to Hess et al. (1998) and Knap et al. (1999).

c. Definition of spectral shape parameter

In order to find a suitable criterion for the determination of the cloud phase, spectra of R_λ between 1.4 and 1.9 μm were simulated for the two cloudy atmospheres described in the previous section. Figure 2 shows the result of these calculations. As indicated by the arrows, the figure shows that the characteristic absorption structure of water and ice seen in Fig. 1 indeed shows up in the simulated reflectivity spectra of the water and ice clouds. Obviously, the minimum in the refractive index of water corresponds to a maximum in R_λ for the water cloud, and the negative slope in the refractive index of ice corresponds to a positive slope in R_λ for the ice cloud. This brings us to the following definition of the so-called spectral shape parameter $S_{1.67}$ (in %):

$$S_{1.67} = 100\frac{R_{1.70} - R_{1.64}}{R_{1.64}}, \qquad (2)$$

where the indices refer to wavelengths in micrometers. Apart from a constant, the numerator is the spectral

TABLE 1. Properties of cloudy atmospheres used for the radiative transfer calculations presented in section 2. Furthermore, this table shows the surface albedo and the viewing and solar geometry used for the simulations.

Parameter	Atmosphere containing water cloud	Atmosphere containing ice cloud	Atmosphere containing mixed-phase cloud
Cloud altitude range	2–3 km	8–9 km	5–6 km
Cloud particle	Spherical water droplet	Imperfect hexagonal ice crystal	Mixture of droplets and crystals
Cloud particle size	$r_{\text{eff}} = 10\ \mu\text{m}$,[a] $v_{\text{eff}} = 1/9$[a]	$L = 60\ \mu\text{m}$,[b] $D = 44\ \mu\text{m}$[b]	Combined size
Cloud optical thickness		10 (Fig. 2), variable (Figs. 3–7)	
Atmospheric profile		Midlatitude summer[c]	
Surface reflectivity (ocean)		0.03 (1.64–1.70 μm)	
Surface reflectivity (vegetation)		0.25 (1.64–1.70 μm)	
Surface reflectivity (snow)		0.20 (1.64 μm), 0.26 (1.70 μm)	
Solar zenith angle		30° (Figs. 3, 5, and 7a), variable (Fig. 4), 60° (Fig. 7b)	
Viewing zenith angle		0° (nadir)	

[a] The particle size distribution for the water cloud is characterized by a two-parameter Γ function with effective radius and variance indicated by r_{eff} and v_{eff}, respectively.

[b] Here, L and D are the length and diameter of the hexagon, respectively. The values given here correspond to crystal type C2 as mentioned in the COP data library (Hess and Wiegner 1994). No size distribution has been used for the calculations for ice clouds.

[c] The midlatitude summer atmosphere for temperature and pressure was taken from Anderson et al. (1986).

FIG. 2. Radiative transfer calculations of TOA reflectivity as a function of wavelength, for an atmosphere with a water cloud ($\tau_{\text{wat}} = 10$) consisting of spheres and for an atmosphere with an ice cloud ($\tau_{\text{ice}} = 10$) consisting of imperfect hexagonal ice columns. The governing characteristics of the cloudy atmospheres are listed in Table 1, together with information about the surface and the solar and viewing geometries. The arrows indicate that the characteristic absorption structure of water and ice as seen in Fig. 1 shows up in the simulated reflectivity spectra of the water and ice clouds.

slope ($dR_\lambda/d\lambda$) at 1.67 μm approximated by a finite difference. For comprehension of Eq. (2), it is important to note that the scattering properties (i.e., the phase functions) of water and ice particles are virtually constant over the wavelength range 1.64–1.70 μm, irrespective of the precise (ice) particle shape. So by dividing by $R_{1.64}$, a relative spectral slope is created that depends primarily on absorption differences over the mentioned wavelength range, because the characteristics of the phase function cancel in the ratio. Since the absorption differences are directly related to the bulk ice volume in the cloud, the cloud phase can be determined by means of thresholding $S_{1.67}$ (see section 2h). For the simulated spectra presented in Fig. 2, it is found that $S_{1.67} = 20\%$ for the ice cloud ($R_{1.64} = 0.29$ and $R_{1.70} = 0.35$) and $S_{1.67} = 0\%$ for the water cloud. The large value of $S_{1.67}$ is due to the fact that in this particular case the ice cloud is optically thick, which makes it easy to distinguish from the water cloud.

d. Calculations for single-layered cloud systems over ocean

As argued in the previous section, the spectral shape parameter $S_{1.67}$ depends primarily on the absorption difference across the 1.64–1.70-μm wavelength range. This difference depends on cloud properties such as optical thickness and crystal size (both related to the bulk ice volume in the cloud) but also on external factors such as solar and viewing geometry. In order to investigate these dependencies, $S_{1.67}$ is shown as a function of ice-cloud optical thickness (τ_{ice}) for different crystal sizes (Fig. 3) and as a function of the solar zenith angle

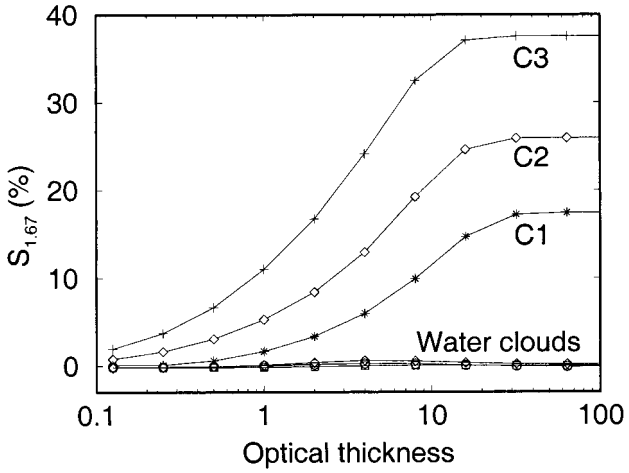

FIG. 3. Radiative transfer calculations of the spectral shape parameter $S_{1.67}$ [Eq. (2)] as a function of cloud optical thickness for atmospheres containing water or ice clouds over ocean. The calculations for water clouds were performed for spherical water droplets with effective radii of 5, 10, and 15 μm. The calculations for ice clouds were performed for imperfect hexagonal columns of different size and shape. The lengths of the hexagons are 30, 60, and 130 μm, and the diameters are 20, 44, and 62 μm, for C1, C2, and C3, respectively. Standard water- and ice-cloud characteristics are given in Table 1.

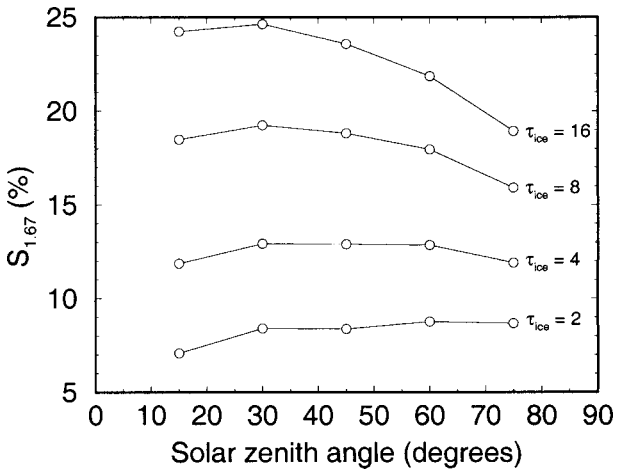

FIG. 4. Radiative transfer calculations of $S_{1.67}$ as a function of solar zenith angle for C2 ice clouds over ocean. The calculations are shown for ice-cloud optical thickness τ_{ice} = 2, 4, 8, and 16. Water- and ice-cloud characteristics are given in Table 1.

for clouds with different τ_{ice} (Fig. 4). Figure 3 also shows $S_{1.67}$ as a function of water-cloud optical thickness (τ_{wat}). As expected, $S_{1.67}$ is close to 0 for all values of τ_{wat}. In order to show that for water clouds over ocean, $S_{1.67}$ does not depend on the cloud droplet size, calculations were repeated for effective radii of 5 and 15 μm. The range of $S_{1.67}$ for all values of τ_{wat} (0.125–128) and all effective radius values (5–15 μm) amounts to between -0.2% and 0.6% (average is 0.03%). For the ice clouds, $S_{1.67}$ varies asymptotically between the two extremes of optical thickness: for $\tau_{ice} \to 0$, $S_{1.67}$ approaches the clear-sky value ($S_{1.67} \to 0$) and for $\tau_{ice} \to \infty$, $S_{1.67}$ approaches a value distinctly different from 0. The latter value depends on the crystal size: the smallest crystals (COP type C1) give the smallest value ($S_{1.67}$ = 17%) and the largest crystals (COP type C3) give the largest value ($S_{1.67}$ = 38%). The ice cloud consisting of crystals of COP type C2 (which was used for the calculation of the R_λ spectrum shown in Fig. 2) gives $S_{1.67}$ = 26%. In the limit of $\tau_{ice} \to \infty$, the ice cloud completely masks the surface, so that the TOA reflectivity spectrum is entirely determined by the radiative properties of the ice cloud. With respect to the dependence of $S_{1.67}$ on cloud optical thickness, it is concluded from Fig. 3 that as the ice cloud becomes optically thicker, the contrast with the water cloud becomes larger and both cloud types can be more easily discriminated from each other.

Figure 4 shows the dependence of $S_{1.67}$ on the solar zenith angle (θ_o) for four ice clouds of different optical thickness. Since the atmosphere is viewed in nadir direction, the given range of θ_o = 15°–75° corresponds to (single) scattering angles between 105° and 165°. Most scattering angles encountered in satellite applications fall within this range. The largest variation in $S_{1.67}$ is seen for τ_{ice} = 16: $S_{1.67}$ decreases by about 6% for θ_o increasing from 30° to 75°. This decrease in $S_{1.67}$ reflects a decrease in the average number of photon scattering events (equivalent to a decrease in photon path length) in the ice-cloud volume for increasing θ_o—when the sun approaches the horizon, photons can escape more easily from the cloud and will consequently penetrate less deeply into the cloud. For optically thinner clouds ($\tau_{ice} \leq 4$) the variation in $S_{1.67}$ is at most 1%–2%. We conclude that the dependence of $S_{1.67}$ on solar (and viewing) geometry is limited, and does not cause problems with respect to the discrimination between water and ice clouds.

e. Calculations for two-layered cloud systems over ocean

In reality, clouds often occur in more than one layer. In order to perform calculations for two-layered cloud systems, a model atmosphere was constructed that contains an ice cloud over a water cloud. The governing characteristics of the cloudy atmosphere are again listed in Table 1. Figure 5 shows calculations of $S_{1.67}$ for an optically thin water cloud (τ_{wat} = 5) and an optically thick water cloud (τ_{wat} = 32) below the ice cloud. The ice-cloud optical thickness is the variable on the *x* axis. In the following discussion, $S_{1.67}$ for the two-layered cloud system is compared with $S_{1.67}$ for the single-layered ice cloud (τ_{wat} = 0). For ice-cloud optical thicknesses greater than 2–3, the enhanced scattering by the water cloud increases $S_{1.67}$ by at most 2%–3% for the thin water cloud and 5% for the thick water cloud. Apparently, the photons reflected by the water cloud increase the average photon pathlength in the ice cloud, so that $S_{1.67}$ increases. For small ice-cloud optical thick-

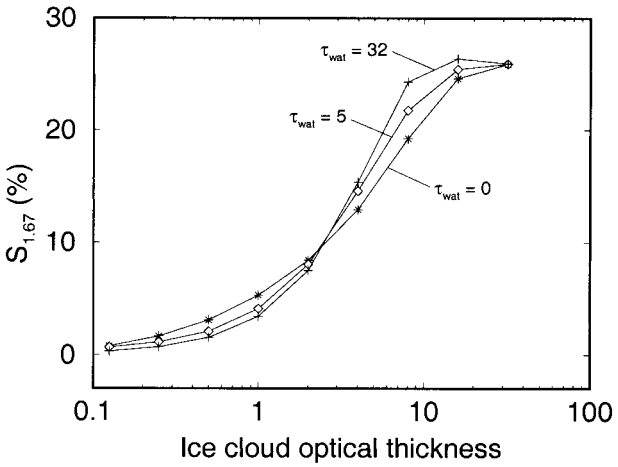

FIG. 5. Radiative transfer calculations of $S_{1.67}$ as a function of ice-cloud optical thickness for an atmosphere containing a two-layered water–ice-cloud system. Water- and ice-cloud characteristics are given in Table 1. Shown are results for an optically thin water cloud ($\tau_{wat} = 5$) and an optically thick water cloud ($\tau_{wat} = 32$) below the ice cloud. For comparison, calculations for a single-layered ice cloud are also shown ($\tau_{wat} = 0$).

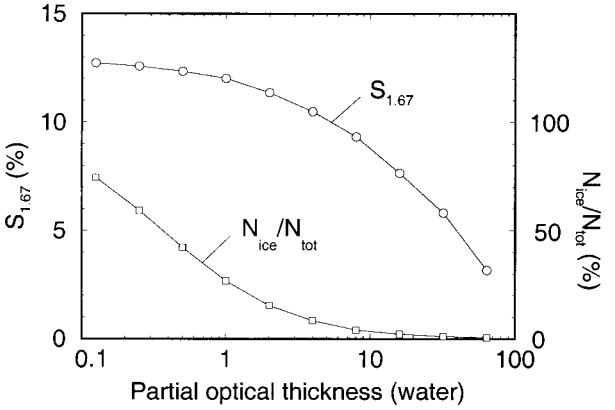

FIG. 6. Radiative transfer calculations of $S_{1.67}$ as a function of partial water-cloud optical thickness for an atmosphere containing a mixed-phase cloud over ocean. On the horizontal axis, from left to right, water droplets (effective radius is 10 μm) are homogeneously mixed into a C2 ice cloud of optical thickness 4. Also shown is the curve for N_{ice}/N_{tot}, that is the number of ice crystals (N_i) relative to the total number of particles (N_{ice}) in the mixed-phase cloud.

ness ($\tau_{ice} < 2$–3) the optical properties of the cloudy atmosphere are dominated by the underlying water cloud, so that $S_{1.67}$ decreases. For increasing water-cloud optical thickness, this decrease is at most 1%–2%. The conclusion is that the presence of ice in a cloud is either accentuated or concealed by an underlying water cloud, depending on the optical thickness of the ice cloud. The degree of accentuation or concealment depends on the optical thickness of the water cloud, and is generally only a few percent in terms of $S_{1.67}$. Consequently, the detection of an ice cloud is not hampered by the presence of an underlying water cloud.

f. Calculations for mixed-phase clouds over ocean

In the previous two paragraphs, calculations have been shown for cloud layers consisting of either water droplets or ice crystals. A single cloud, however, may consist of a mixture of water droplets and ice crystals. In order to investigate how $S_{1.67}$ is influenced by the composition of a mixed-phase cloud, a model ice cloud was constructed into which an increasing number of water droplets were homogeneously mixed. Figure 6 shows calculations of $S_{1.67}$ for a mixed-phase cloud with a fixed partial-ice-cloud optical thickness, $\tau_{ice} = 4$, and a variable partial-water-cloud optical thickness, τ_{wat}. In the same figure, the number of ice crystals (N_{ice}) relative to the total number of cloud particles (N_{tot}) is shown. For $\tau_{wat} \to 0$ the composition of the mixed-phase cloud approaches that of a pure ice cloud of optical thickness 4, so $S_{1.67} \to 13\%$ (cf. Fig. 3). If water droplets are mixed into the ice cloud, $S_{1.67}$ gradually decreases to a few percent for $\tau_{wat} = 60$–70. For larger values of τ_{wat} the mixed-phase cloud almost entirely consists of water droplets, so $S_{1.67} \to 0$ (not shown). It is worth noting that $S_{1.67}$ is very sensitive to a small addition of ice crystals to a water cloud: for $N_{ice}/N_{tot} = 0.6\%$ (the most-right data point in Fig. 6), $S_{1.67}$ is already greater than 3%. Apart from this result, the calculations for mixed-phase clouds show that a certain degree of ambiguity with regard to $S_{1.67}$ is introduced: a mixed-phase cloud of given τ_{wat} and τ_{ice} may have the same spectral shape parameter as a pure ice cloud of different (smaller) τ_{ice}.

g. Calculations for clouds over land

Although this paper primarily deals with cloud-phase determination over ocean, in this section a brief discussion of the possibilities and limitations of cloud-phase determination over land surfaces using the spectral shape parameter $S_{1.67}$ is given. For this discussion it is essential to consider the spectral characteristics of the surface for the 1.67-μm region. To do this, the quantity $S^{sfc}_{1.67}$ is introduced, which is the analogy of $S_{1.67}$ but now for spectral surface reflectivities. Note that $S_{1.67}$ is close to $S^{sfc}_{1.67}$ in the limit of zero cloud optical thickness. For ocean, $S^{sfc}_{1.67} \approx 0$, which is a direct consequence of the typical absorption structure of liquid water (Fig. 1). For green vegetation, it also appears that $S^{sfc}_{1.67} \approx 0$. This is due to the fact that, beyond 1.3 μm, the reflectivity of photosynthetically active vegetation is primarily controlled by leaf water content (Bowker et al. 1985). The broad water absorption areas near 1.4 and 1.95 μm cause $S^{sfc}_{1.67}$ to vanish. In this respect, it is essential to note that surface types for which $S^{sfc}_{1.67} \approx 0$, such as green vegetation, basically give the same relationship between $S_{1.67}$ and cloud optical thickness as shown for ocean in Fig. 3. This is confirmed by Fig. 7a, which shows calculations of $S_{1.67}$ for C2 ice clouds and water clouds over both ocean and green vegetation. The spectral surface

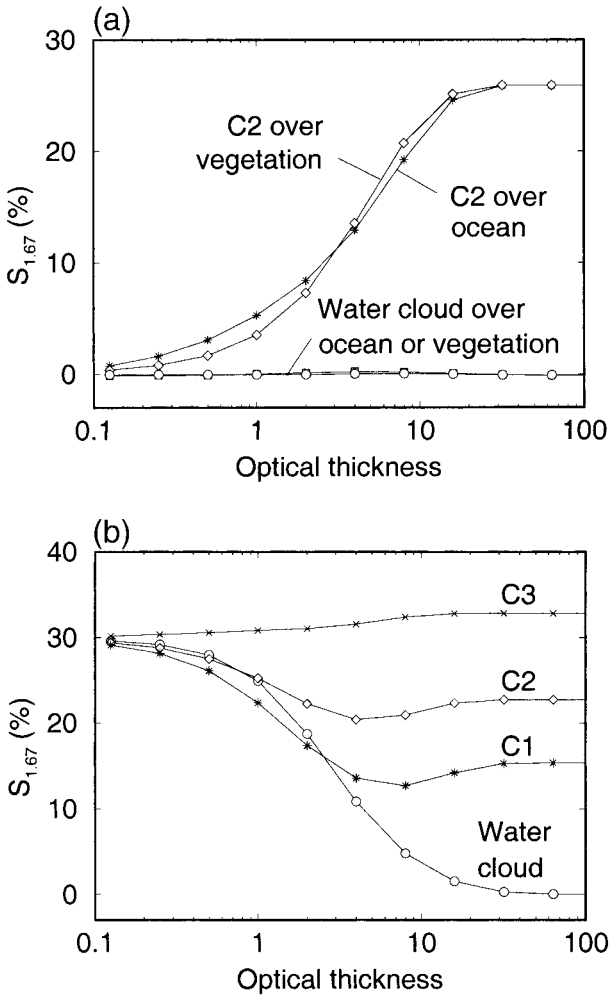

FIG. 7. (a) Calculations of $S_{1.67}$ as a function of cloud optical thickness for water and C2 ice clouds over ocean and green vegetation. For green vegetation $R_{1.67} = 0.25$ and $S^{sfc}_{1.67} = 0$ (Bowker et al. 1985). (b) The same as Fig. 3, but for clouds over a fine-grained snow surface (effective grain radius is 50 μm) with $R_{1.64} = 0.20$ and $R_{1.70} = 0.26$ ($S^{sfc}_{1.67} = 30\%$; Wiscombe and Warren 1980).

characteristics for typical vegetation were taken from Bowker et al. (1985; $R_{1.67} = 0.25$ and $S^{sfc}_{1.67} = 0$). Apparently, the behavior of $S_{1.67}$ for an ice cloud over vegetation is very similar to that of an ice cloud over a water cloud (compare Figs. 7a and 5).

According to Bowker et al. (1985), the reflectivity of vegetation usually progresses from a background, such as soil, to full greenness and then returns to the background again. Although, $S^{sfc}_{1.67}$ is close to 0 for most soil, dry soil typically has values of $S^{sfc}_{1.67}$ greater than 0, which may complicate a proper cloud-phase determination. A similar statement can be made for rocks and minerals, which are similar to soil in reflectivity.

Snow is probably the most complicating surface because of the optical similarities between a snow cover and an ice cloud. To illustrate this, calculations for ice clouds over a surface consisting of pure fine-grained snow (effective grain radius is 50 μm) were performed. The value of $S^{sfc}_{1.67}$ for this type of snow was derived from calculations of the spectral albedo of pure snow performed by Wiscombe and Warren (1980): $S^{sfc}_{1.67} \approx 30\%$. This value is close to the values of $S_{1.67}$ for optically thick ice clouds consisting of type C2 and C3 crystals (cf. Fig. 3). Calculations of $S_{1.67}$ for ice clouds and water clouds over the fine-grained snow pack are shown in Fig. 7b. As can be seen in this figure, $S_{1.67}$ varies between the surface value of 30% (for $\tau_{ice} \to 0$ or $\tau_{wat} \to 0$) and the different values for optically thick clouds.[1] The most important conclusion that can be drawn from this figure is that for cloud optical thicknesses less than about 2–4 it is not possible to separate ice clouds from water clouds on the basis of the magnitude of $S_{1.67}$ because the curves for water and ice clouds are twisted.

In conclusion it is stated that the spectral shape parameter $S_{1.67}$ is, in principle, suitable for cloud-phase determination over spectrally neutral surfaces (i.e., surfaces for which $S^{sfc}_{1.67} \approx 0$), such as ocean and green vegetation. Ambiguities occur in cases where optically thin clouds are present over, for example, mineral, rock, (dry) soil, or snow surfaces.

h. Cloud detection and cloud-phase determination over ocean

In order to test the principle of cloud-phase determination put forward in sections 2a–c by means of AVIRIS measurements, in this section a simple cloud-phase determination algorithm for clouds over ocean is presented. The measurements to be analyzed in section 3 consist of a partly overlapping two-layered water–ice cloud system, so the basis of the algorithm described here is found in the calculations presented in sections 2c–e.

Since $S_{1.67} \approx 0$ for both an atmosphere containing a water cloud and a clear atmosphere over a water surface, these two cases cannot be distinguished from each other using the shape of the reflectivity spectrum. So, prior to determining the cloud phase, the cloud itself needs to be identified. Since cloud-phase determination, rather than cloud detection, is the main topic of this paper, a simple cloud-detection algorithm is presented (left part of Fig. 8), which is suitable for analysis of the measurements made over ocean presented later in this paper. The basis of this algorithm is a comparison of the measured reflectivity R with a clear-sky reference R_{clr}. If $R \leq R_{clr}$ then the pixel under consideration is clear, otherwise it is cloudy. For the comparison it is important to select a wavelength for which there is a large contrast

[1] Note that the values of $S_{1.67}$ for optically thick ice clouds over snow are slightly different from the corresponding values seen in Fig. 3. This is caused by a difference in solar zenith angle: $\theta_o = 30°$ for the calculations over ocean and $\theta_o = 60°$ for the calculations over snow.

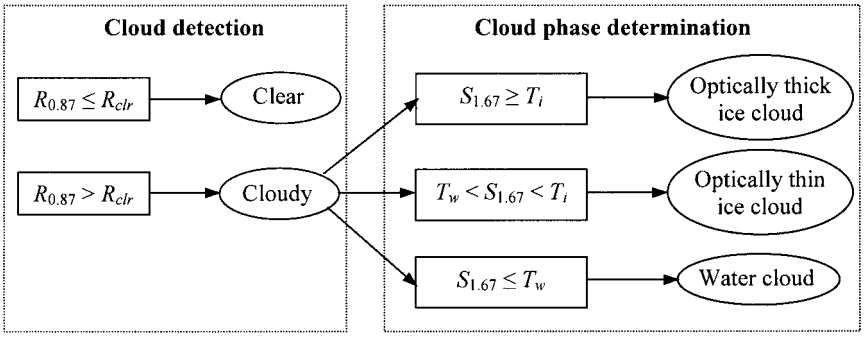

FIG. 8. Schematic representation of the cloud-detection algorithm and (right) the cloud-phase-determination algorithm for clouds over ocean. The former is based on thresholding the reflectivity at 0.87 μm ($R_{0.87}$) relative to a clear sky value at this wavelength (R_{clr}). The cloud-phase-determination algorithm is based on thresholding the spectral shape parameter $S_{1.67}$ with two thresholds: T_w and T_i.

for R between the clear and cloudy atmosphere. For cloudy atmospheres over ocean, wavelengths shorter than about 1.3 μm are suitable, although wavelengths shorter than 0.6 μm should be avoided because of Rayleigh scattering, as well as spectral regions where gaseous absorption is important. For the cloud detection to be discussed in section 3e, the reflectivity at 0.87 μm is used.

The cloud-phase-determination algorithm is based on two thresholds for $S_{1.67}$, T_w and T_i, which define three classes: 1) $S_{1.67} \le T_w$, 2) $T_w < S_{1.67} < T_i$, and 3) $S_{1.67} \ge T_i$. A schematic representation of the algorithm is given in Fig. 8 (right part). The first class consists of atmospheres containing water clouds. Although the radiative transfer calculations for these atmospheres predict that $S_{1.67} = 0$ (Fig. 2), it is necessary to allow for some tolerance because of factors such as spectrometer-channel bandwidth at 1.64 and 1.70 μm and (uncertainty in) wavelength center position. These factors cause $R_{1.70} - R_{1.64}$ to be not precisely 0, even if the real reflectivity spectrum would suggest the opposite. Additionally, absorption by CO_2 causes the water-cloud spectrum to be not as smooth as predicted by the radiative transfer calculations. As will be shown in section 3e, a value of T_w can be obtained from a measured distribution of $S_{1.67}$ over a cloud which is known to consist of water droplets. The second class consists of atmospheres containing optically thin ice clouds. The upper limit for ice cloud optical thickness in this class depends on the choice of T_i, and on the crystal size within the ice cloud (see Fig. 3). For the present study, a value of T_i was obtained using information contained in the 1.38-μm AVIRIS water vapor absorption image (section 3e). Since ice clouds within this class are optically thin, the properties of an underlying water cloud may have influence on the magnitude of $S_{1.67}$ (see section 2e). In this context it should be noted that on the basis of the magnitude of $S_{1.67}$ it is not possible to decide whether one is dealing with a one- or two-layered cloud system. The third class consists of atmospheres containing optically thick ice clouds. For this class, the magnitude of $S_{1.67}$ is primarily determined by the ice-cloud properties and possible underlying water clouds have negligible influence on the magnitude of $S_{1.67}$.

3. AVIRIS Measurements

a. Introduction

In order to evaluate the radiative-transfer calculations and the cloud-phase-determination algorithm presented in the previous section, AVIRIS (Green et al. 1998) measurements made over a cloud system over the Pacific Ocean on 2 June 1995 were selected. AVIRIS is an imaging spectrometer that measures the upwelling radiance in 224 contiguous spectral channels at 10-nm intervals from 0.4 to 2.5 μm. The spectral resolution is also 10 nm, which is sufficient for the detection of the absorption structure described in section 2c. AVIRIS flies aboard a National Aeronautics and Space Administration Earth Resources-2 (ER-2) aircraft at 20 km above sea level. At this altitude the spatial resolution of AVIRIS is 20 m. Images measure 11 km in width and up to 800 km in length. An in-flight calibration experiment for 1995 (Green et al. 1996) showed that the AVIRIS radiometric calibration error is smaller than 3.5%. For wavelengths around 1.6 μm, the signal-to-noise ratio was around 500. The spectral calibration accuracy is better than 1 nm (Green et al. 1998). For further details about AVIRIS the reader is referred to Green et al. (1998).

b. Selection of data

Figure 9a shows the selected image at 0.87 μm. From bottom to top, the image contains stratocumulus (Sc) clouds, cirrus (Ci) clouds, an area of thin cirrus, another tuft of thicker cirrus, a narrow area of stratocumulus (top right side of the image), followed by a clear area outside the selection showed here. The information on

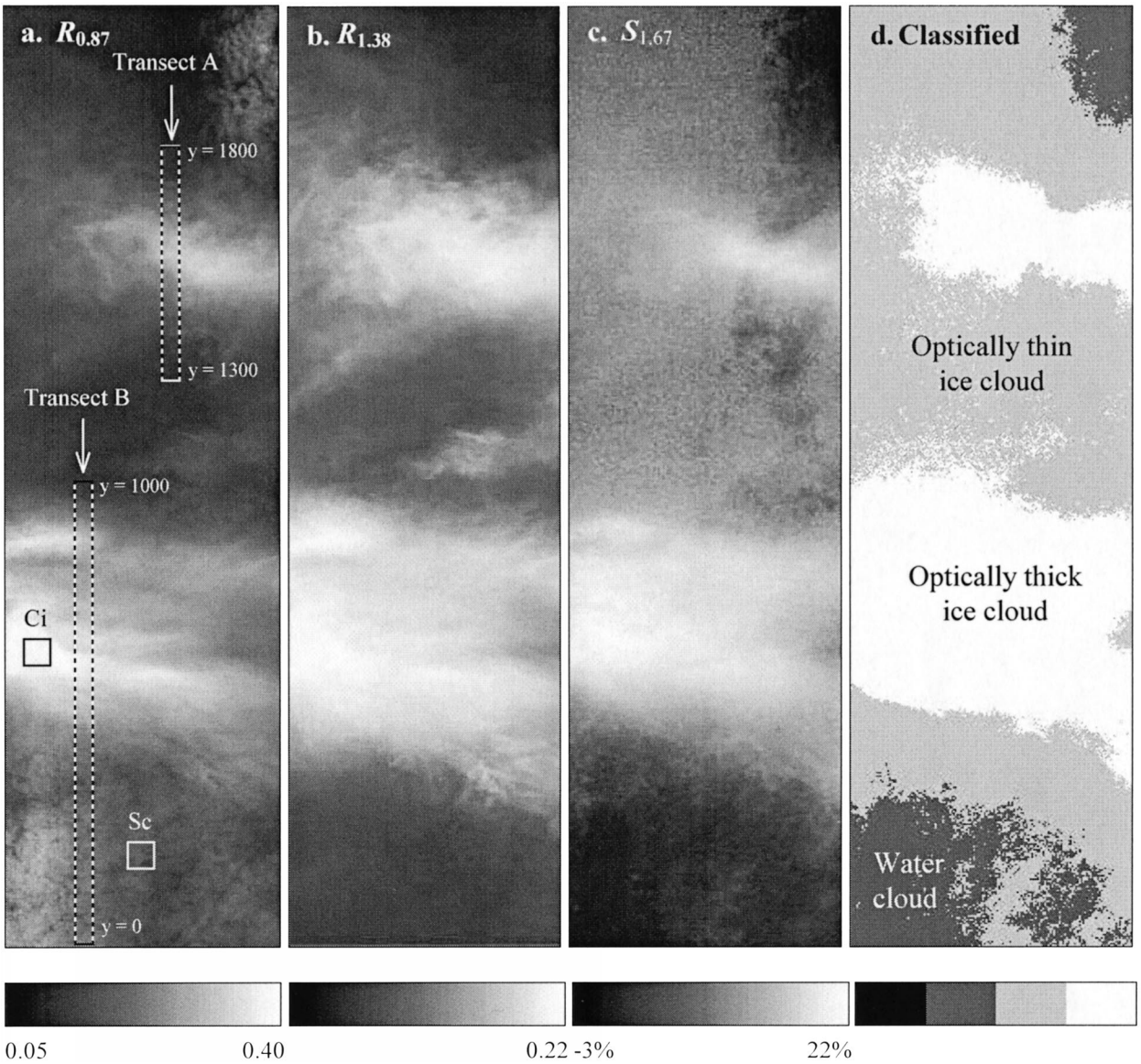

FIG. 9. (a) Selection of AVIRIS image 950602C0101, site name ''Cloud Data,'' shown for the 0.87-μm wavelength. The image has been acquired over the Pacific Ocean (48°N, 128°W), about 300 km west of Port Angeles, Washington, on 2 Jun 1995. The solar zenith angle at the time of the overpass is 31°. For the analysis presented here, two homogeneous cloudy areas (''Ci'' and ''Sc'') and one clear ocean area (outside the part of image that is shown here) are selected. Transect A extends over gradually thickening and thinning Ci, whereas transect B contains both Sc and Ci of variable optical thickness. The variable y indicates the along-track pixel coordinate. (b) The same image as in (a) but for 1.38 μm (water vapor absorption band). (c) The same image as in (a) but for $S_{1.67}$. (d) The same image as in (a) but arranged into classes according to the cloud-phase-determination algorithm shown in Fig. 8. The thresholds used are $T_w = 2\%$, $T_i = 10\%$, and $R_{\text{clr}} = 0.03$.

cloud type was obtained from the ER-2 pilot in combination with visual interpretation of the cloud structures seen in Figs. 9a and 9b (the latter to be discussed below). Stratocumulus clouds are low-level clouds (cloud base usually below 2 km) with warm base temperatures (5°–10°C in maritime areas) and consist predominantly of liquid water droplets (Heymsfield 1993). Cirrus clouds, however, are situated higher in the atmosphere (in the midlatitudes, typically between 6 and 9 km) and consist almost exclusively of ice crystals. Both cloud types have horizontal dimensions that are much greater than their vertical extent and occur in layers of several hundred meters (for Sc and mid- and low-latitude Ci). The fact that the AVIRIS image contains low- and high-level clouds can well be illustrated by displaying it at 1.38 μm (Fig. 9b). This wavelength is situated in a strong water vapor absorption band, so that radiation from the lower troposphere is almost entirely absorbed by water vapor. The result is that AVIRIS detects at this wavelength almost only the Ci clouds,

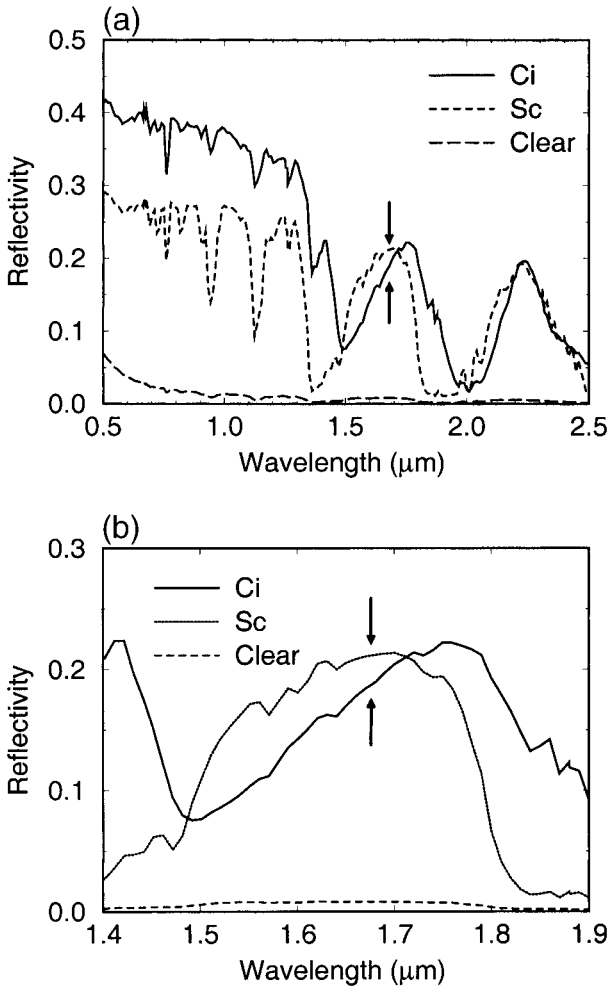

FIG. 10. (a) Mean AVIRIS spectra for the Sc and Ci areas (locations indicated in Fig. 9a), and for a clear ocean area. Each spectrum is the average of 31 × 31 pixels, which corresponds to an area of about 600 × 600 m². At 1.67 μm (indicated by the arrows) there is a clear shape difference in the spectra for water and ice clouds (cf. Fig. 10b). (b) The same as Fig. 10a, but zoomed in at wavelengths between 1.4 and 1.9 μm.

which can been seen in Fig. 9b. This figure also shows that the 1.38-μm channel detects a weak signal ($R_{1.38} \approx 0.02$) in the lowest part of the image, which may indicate the presence of very thin cirrus. It is also possible that the signal from the Sc cloud is not entirely suppressed by water vapor absorption. Gao et al. (1993) state that the 1.38-μm channel has some sensitivity to midlevel clouds (top altitudes between 3 and 6 km). Therefore, one may speculate that the Sc cloud under consideration is high and dense enough to be responsible for this weak signal.

Another argument for the presence of water clouds in the AVIRIS image is found in the fact that the reflectivity of the Sc cloud in the lower left corner of the image is substantially larger than over other parts of the cloud (Fig. 9a). This area of enhanced reflectivity corresponds to scattering angles around 135°, which indicates that a cloudbow is observed and that the lower part of the image indeed consists of water clouds.

For the analysis presented here, two square cloudy areas of 31 × 31 pixels (~600 m × 600 m) and two cloudy transects of 500 × 10 pixels (~10 km × 0.2 km) and 1000 × 10 pixels (~20 km × 0.2 km) were selected. In Fig. 9a the cloudy areas are indicated by Sc, Ci, transect A, and transect B. The first two areas are, with respect to reflectivity, relatively homogeneous and contain optically thick stratocumulus (Sc) and cirrus (Ci). Transect A extends over gradually thickening and thinning Ci, whereas transect B contains both Sc and Ci of variable optical thickness. Besides the cloudy areas, a third square area of 31 × 31 pixels was selected which contains no clouds at all. This area is situated outside the image shown in Fig. 9a.

c. Analysis of AVIRIS spectra

For each pixel of the areas described above, the AVIRIS spectral reflectivity R_λ at the center wavelength λ was calculated according to Eq. (1). The calibrated radiance L_λ was calculated from the raw image data and the multiplication factors for radiometric calibration, which are supplied with the data. Here, $S_{o,\lambda}$ is the convolution of the solar spectral irradiance (ESA 1994) and the AVIRIS slit function, which was approximated by a Gaussian function (the standard deviations are supplied with the AVIRIS data).

Area-averaged spectra of R_λ of the Sc and Ci areas are shown in Fig. 10a. For comparison, a spectrum of the clear-ocean area is also shown. The absorption bands of gases such as H_2O and O_2 can clearly be recognized by strong reductions in cloud reflectivity. For wavelengths shorter than about 1.5 μm the ice cloud is significantly brighter than the water cloud, which may be caused by a difference in optical thickness between the two clouds. The difference in brightness could also be due to the fact that ice crystals scatter more radiation in the sideward direction than water droplets.

In order to compare the radiative transfer calculations of R_λ for typical water and ice clouds (Fig. 2) with the AVIRIS spectra of the Sc and Ci clouds, the measured spectra are considered for wavelengths between 1.4 and 1.9 μm (Fig. 10b). The figure shows clearly that the typical 1.67-μm absorption structure seen in the calculations of R_λ is also present in the AVIRIS spectra: the spectrum for the Sc cloud has approximately a zero slope and the spectrum for the Ci cloud has a distinct positive slope. The agreement between the radiative transfer calculations and the AVIRIS measurements implies that the principle of using the shape of the reflectivity spectrum around 1.67 μm for the determination of the thermodynamic cloud phase is basically correct.

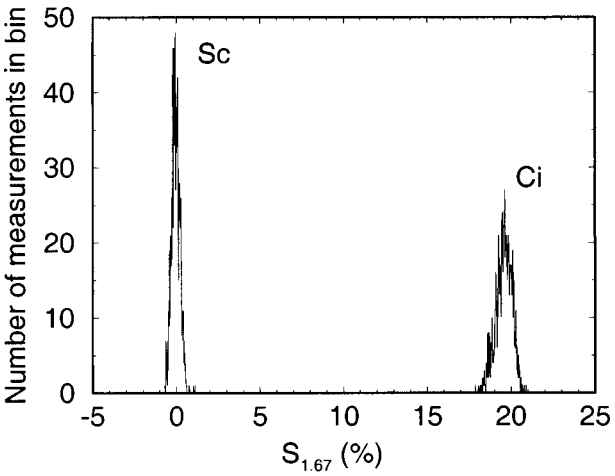

FIG. 11. Frequency distributions of the spectral shape parameter $S_{1.67}$ derived from AVIRIS measurements for the two cloudy areas shown in Fig. 9a. Each histogram is made up of 31 × 31 AVIRIS pixels. The corresponding area-averaged spectra are shown in Figs. 10a and 10b.

d. Spectral shape parameter for AVIRIS measurements

The irregularities in the cloud spectra for wavelengths between 1.55 and 1.75 μm (Fig. 10b), which are caused by CO_2 absorption, interfere with the determination of spectral shape parameter $S_{1.67}$. Therefore, a seven-point running mean was applied to smooth the AVIRIS cloud spectra prior to determining $S_{1.67}$. In order to obtain reflectivities at the correct wavelengths, AVIRIS channels 136 and 142 are used (wavelength center positions at 1.64 and 1.70 μm, respectively) to calculate $S_{1.67}$. Frequency distributions of $S_{1.67}$ for the Sc and Ci areas are shown in Fig. 11. The separation between water and ice cloud is obvious: $S_{1.67}$ for the Sc field peaks at values close to zero (average: −0.03%), whereas $S_{1.67}$ for the Ci field peaks at an average value of 19.6%. Since the distributions do not overlap, the thermodynamic phase of a cloudy pixel in this particular selection of measurements can unambiguously be established on the basis of the magnitude of $S_{1.67}$.

According to the radiative transfer calculations shown in Fig. 3, $S_{1.67} \approx 20\%$ corresponds to an ice cloud with optical thickness of 2–3 (assuming COP type C3 crystals) or larger (assuming smaller crystals). Whatever the precise size of the ice crystals within the observed Ci cloud area is, the optical thickness is apparently large enough to obtain contrasting values of $S_{1.67}$ for the water and ice clouds. However, as the optical thickness of the ice cloud decreases, this contrast decreases. In order to illustrate the dependence of $S_{1.67}$ on ice-cloud optical thickness, $S_{1.67}$ was determined along transect A (cf. Fig. 9a), which extends over gradually thickening and thinning cirrus. The result is shown in Fig. 12a, where both $S_{1.67}$ and $R_{1.67}$ are plotted as a function of the along-track pixel coordinate (indicated by the symbol *y* in Fig. 9a).

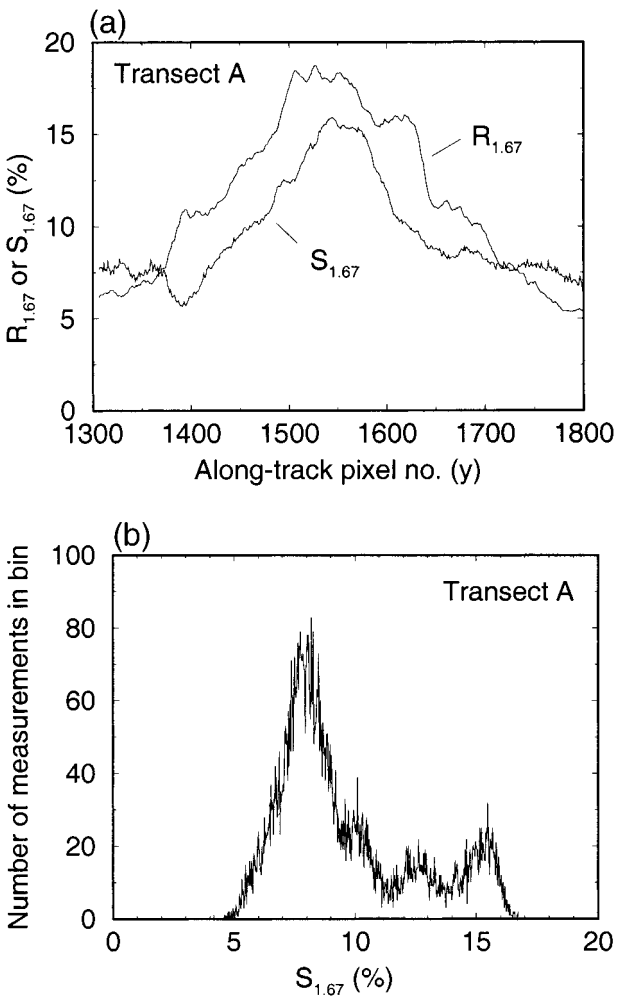

FIG. 12. (a) AVIRIS reflectivity $R_{1.67}$ and spectral shape parameter $S_{1.67}$ along transect A (see Fig. 9a). The *x* axis represents the along-track pixel coordinate *y*. Each data point represents a 10-pixel across-track mean. The length of the transect is about 10 km (500 pixels). The transect extends over an area of gradually thickening and thinning cirrus. (b) Frequency distribution of $S_{1.67}$ for transect A.

The corresponding frequency distribution of $S_{1.67}$ is shown in Fig. 12b. There is virtually no overlap between the distributions for transect A and the Sc area (cf. Fig. 11), which confirms the statement made in section 3a that the cloud in transect A consists of ice crystals. The small values of $S_{1.67}$ at the tails of the transect suggest the presence of optically thin Ci. The presence of thin clouds is also indicated by $R_{1.67}$ itself (Fig. 12a); the lowest values are still substantially higher than the clear-ocean reflectivity, which is less than 0.01 at 1.67 μm (Fig. 10b). If $R_{1.67}$ is considered as a proxy for cloud optical thickness, then Fig. 12a shows an increase in $S_{1.67}$ with increasing Ci optical thickness. This is in agreement with the radiative transfer calculations shown in Fig. 3.

Compared to transect A, the situation for transect B is more complicated because this transect contains areas

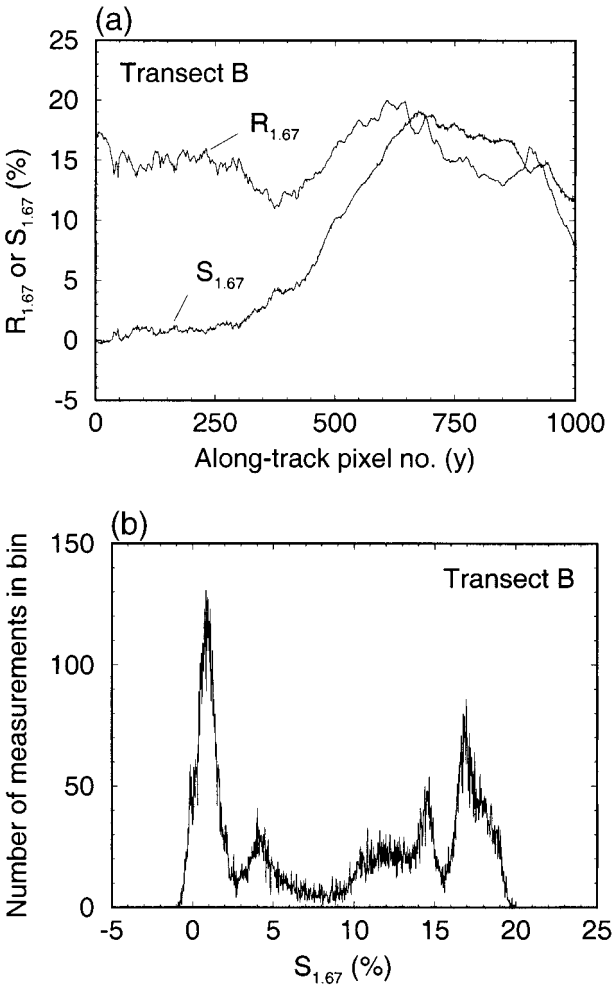

FIG. 13. (a) AVIRIS reflectivity $R_{1.67}$ and spectral shape parameter $S_{1.67}$ along transect B (see Fig. 9a). The x axis represents the along-track pixel coordinate y. Each data point consists of a 10-pixel across-track mean. The length of the transect is about 20 km (1000 pixels). The first part of the transect extends over Sc, the second over Ci. In between, there is an area of optically thin Ci over Sc. (b) Frequency distribution of $S_{1.67}$ for transect B.

of both Sc and Ci, and a transitional zone between both cloud types. In Fig. 13a, $S_{1.67}$ and $R_{1.67}$ are plotted as a function of the along-track pixel coordinate y. The frequency distribution of $S_{1.67}$ for transect B is shown in Fig. 13b. The first peak roughly corresponds to the first 260 pixels of the transect, which covers the Sc cloud. The rest of the frequency distribution contains several peaks, which correspond to clusters of pixels of different optical thickness and/or particle size in the Ci cloud. Between about $y = 260$ and $y = 500$, $S_{1.67}$ gradually increases from 1%–2% to 10% (Fig. 13a). Since the Sc cloud extends below the Ci cloud (AVIRIS pilot information), this part of the transect resembles the two-layered cloud system as described in section 2e. Most probably, the gradual increase in $S_{1.67}$ can be explained by the presence of thin Ci of increasing optical thickness over the Sc cloud.

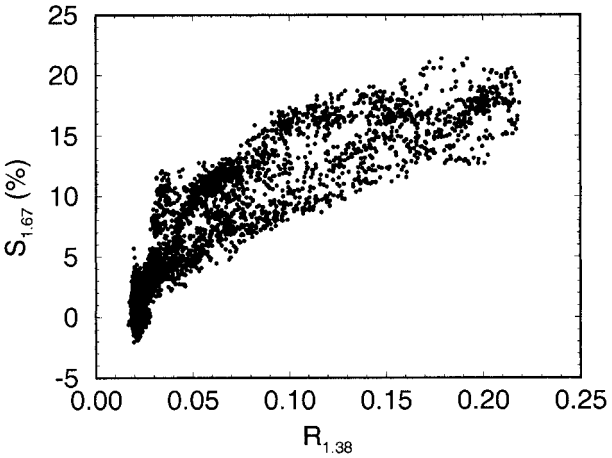

FIG. 14. Correlation between $S_{1.67}$ and $R_{1.38}$ for randomly selected data along transect B (see Fig. 9a). The 1.38-μm wavelength is situated in a strong water-vapor absorption band (see text and Fig. 9b).

In view of the fact that $S_{1.67}$ is sensitive to the presence of ice particles in clouds and that $R_{1.38}$ is sensitive to scattering particles or surfaces situated high in the atmosphere (see section 3b), it is interesting to correlate $S_{1.67}$ with $R_{1.38}$. Figure 14 shows this correlation for a random selection of data along transect B. The general pattern of positive correlation suggests that for the present case both quantities can be used to detect ice clouds. The relationship between $S_{1.67}$ and $R_{1.38}$ resembles a square root function: $S_{1.67} \propto (R_{1.38})^{1/2}$ which implies that for small reflectivities the derivative $dS_{1.67}/dR_{1.38}$ becomes large. Apparently, for the thinnest Ci considered here, $S_{1.67}$ responds more sensitively to the presence of ice than $R_{1.38}$.

e. Classification of the AVIRIS image

On the basis of the cloud-phase-determination algorithm presented in section 2h, and by choosing appropriate values of the thresholds T_w and T_i, and the clear-sky reflectivity R_{clr}, the AVIRIS image can be arranged into the different classes according to cloud thermodynamic phase. According to the distribution of $S_{1.67}$ for Sc clouds, $S_{1.67}$ is less than 1% for this selection of water clouds (Fig. 11). In order to allow for some tolerance, for the first threshold, twice this value was chosen: $T_w = 2\%$. According to the calculations for two-layered clouds shown in Fig. 5, this lower threshold for optically thin ice clouds corresponds to a C2 ice-cloud optical thickness of about 0.5–0.6 (note that this value is different for smaller or larger ice crystal sizes). According to the 1.38-μm water vapor absorption image (Fig. 9b), the Ci cloud extends roughly from $y = 500$ to $y = 1000$. On the basis of Fig. 13a, it is then found that $T_i = 10\%$ is a reasonable choice for defining the class of optically thick ice clouds ($S_{1.67} \geq T_i$). Since the clear-sky reflectivity over ocean is generally less than 0.02 at 0.87 μm, $R_{\text{clr}} = 0.02$. Figure 9c shows the values of $S_{1.67}$ in the

AVIRIS image and Fig. 9d shows the classified image according to $T_w = 2\%$ and $T_i = 10\%$. By comparing Figs. 9b ($R_{1.38}$) and c ($S_{1.67}$), it can be seen that the Ci clouds clearly show up as bright areas where $S_{1.67}$ is significantly greater than zero. This leads to a clear identification of the Ci clouds by the cloud-phase-determination algorithm (Fig. 9d). The classified image also shows a relatively large area with values of $S_{1.67}$ between T_w and T_i (class is optically thin ice cloud). For an ice cloud consisting of crystals of COP type C2, these values correspond to ice-cloud optical thicknesses of 0.3–2.6 (cf. Figs. 3 and 4). On the basis of the location of Sc clouds in Fig. 9a, it can be concluded that the cloud-phase-determination algorithm performs also well in identifying water clouds: in the lower part of the image the Sc clouds are clearly present, even though some areas suggest the presence of thin Ci overlying the Sc cloud.

Obviously, the sensitivity of the algorithm to the occurrence of the different cloud types, and in particular to (optically thin) ice clouds, depends on the choice of the thresholds T_w and T_i. For example, the extensive area of optically thin ice clouds in the lower part of Fig. 9d can be reduced by increasing T_w by a few percent. With respect to the presence of Sc clouds seen in Fig. 9a, this will lead to better visual agreement between Figs. 9a and 9d. On the other hand, one should bear in mind that the great sensitivity of the method to the presence of ice particles in clouds offers an excellent opportunity for detecting optically thin ice clouds.

4. Conclusions

The analysis of the AVIRIS measurements confirms our idea obtained from radiative transfer calculations that the shape of the cloud reflectivity spectrum around 1.67 μm [expressed in terms of the spectral shape parameter $S_{1.67} = 100(R_{1.70} - R_{1.64})/R_{1.64}$] offers an effective means of determining the thermodynamic phase of clouds over ocean from imaging-spectrometer data covering wavelengths around 1.67 μm. Important aspects of the cloud-phase-determination algorithm presented here are the great sensitivity of $S_{1.67}$ to the presence of ice particles in clouds, and the weak dependence of this parameter on viewing and solar geometry.

The most important differences between instrument characteristics of the airborne AVIRIS and the spaceborne SCIAMACHY are the spectral resolution (10 and 1 nm, respectively) and the spatial resolution (20 m and several tens of kilometers, respectively). As for the spectral resolution, the redundant spectral information, which is related to gaseous absorption and which interferes with a proper determination of $S_{1.67}$, can easily be removed by omitting gas absorption lines in measured spectra and by spectral averaging of radiances. The reduced spatial resolution of SCIAMACHY as compared to AVIRIS is likely to cause less extreme values of $S_{1.67}$ because of the fact that more frequently both water and ice clouds will occur in the same pixel. Therefore, the change of horizontal scale is an aspect that has to be taken into account when interpreting future cloud phase products to be derived from SCIAMACHY.

The evaluation of the cloud-phase-determination method presented here has been confined to the relatively simple situation of vertically separated cloud layers over an ocean surface. On the basis of radiative transfer calculations for mixed-phase clouds it has been shown that, by using $S_{1.67}$ as criterion, these clouds cannot be distinguished from pure ice clouds. In this respect it should be noted that the identification of mixed-phase clouds in satellite imagery is a common problem (see e.g., Key and Intrieri 2000) that needs further research. It has furthermore been shown that our method may lead to misclassifications in cases where optically thin clouds are present over snow. It is suggested that this also applies to minerals, rocks, and (dry) soils. On the other hand, it has been shown that there is no fundamental difference between $S_{1.67}$ cloud-phase determination over ocean and green vegetation (note that this does not necessarily apply to cloud detection). In view of this, and because of the fact that the cloud types considered in this paper (stratocumulus and cirrus) are widespread in the earth's atmosphere, the algorithm presented here provides a suitable basis for cloud-phase determination over large parts of the globe using near-infrared reflectivity spectra of clouds.

Acknowledgments. Financial support for this research was provided by the Space Research Organization Netherlands Project EO-025. The comments of three anonymous reviewers are gratefully acknowledged. Thanks are due to Stephen Warren at the University of Washington in Seattle for providing the calculations for the spectral albedo of snow.

REFERENCES

Anderson, G. P., S. A. Clough, F. X. Kneizys, J. H. Chetwynd, and E. P. Shettle, 1986: AFGL atmospheric constituent profiles. Air Force Geophysics Laboratory Tech. Rep. AFGL-TR-86-0110, 43 pp.

Baum, B. A., P. F. Soulen, K. I. Strabala, M. D. King, S. A. Ackerman, W. P. Menzel, and P. Yang, 2000: Remote sensing of cloud properties using MODIS airborne simulator imagery during SUCCESS. 2. Cloud thermodynamic phase. *J. Geophys. Res.*, **105,** 11 781–11 792.

Bovensmann, H., J. P. Burrows, M. Buchwitz, J. Frerick, S. Noël, V. V. Rozanov, K. V. Chance, and A. P. H. Goede, 1999: SCIAMACHY: Mission objectives and measurement modes. *J. Atmos. Sci.*, **56,** 127–150.

Bowker, D. E., R. E. Davis, D. L. Myrick, K. Stacy, and W. T. Jones, 1985: Spectral reflectances of natural targets for use in remote sensing studies. NASA Reference Rep. 1139, 184 pp.

C.-Labonnote, L., G. Brogniez, J.-C. Buriez, M. Doutriaux-Boucher, J.-C. Gayet, and A. Macke, 2001: Polarized light scattering by inhomogeneous hexagonal monocrystals. Validation with ADEOS–POLDER measurements. *J. Geophys. Res.*, **106,** 12 139–12 153.

de Haan, J. F., P. Bosma, and J. W. Hovenier, 1987: The adding method

for multiple scattering calculations of polarized light. *Astron. Astrophys.,* **183,** 371–391.

de Rooij, W. A., and C. C. A. H. Van der Stap, 1984: Expansion of Mie scattering matrices in generalized spherical functions. *Astron. Astrophys.,* **131,** 237–248.

Doutriaux-Boucher, M., J.-C. Buriez, G. Brogniez, L. C.-Labonnote, and A. J. Baran, 2000: Sensitivity of retrieved POLDER directional cloud optical thickness to various ice particle models. *Geophys. Res. Lett.,* **27,** 109–112.

Downing, H. D., and D. Williams, 1975: Optical constants of water in the infrared. *J. Geophys. Res.,* **80,** 1656–1661.

ESA, 1994: Study of Sun and Moon as radiation targets. ESA Contract Rep. SSF-ESA-SM-0002, 144 pp.

Gao, B.-C., A. F. H. Goetz, and W. J. Wiscombe, 1993: Cirrus cloud detection from airborne imaging spectrometer data using the 1.38 μm water vapor band. *Geophys. Res. Lett.,* **20,** 301–304.

Green, R. O., J. E. Conel, J. Margolis, C. Chovit, and J. Faust, 1996: In-flight calibration and validation of the Airborne Visible/Infrared Imaging Spectrometer (AVIRIS). *Proc. Eighth Annual JPL Airborne Earthscience Workshop,* Pasadena, CA, Jet Propulsion Laboratory, 115–126.

——, and Coauthors, 1998: Imaging spectroscopy and the Airborne Visible Infrared Imaging Spectrometer (AVIRIS). *Remote Sens. Environ.,* **65,** 227–248.

Hale, G. M., and M. R. Querry, 1973: Optical constants of water in the 200 nm to 200 μm wavelength region. *Appl. Opt.,* **12,** 555–563.

Hartmann, D. L., 1993: Radiative effects of clouds on Earth's climate. *Aerosol-Cloud-Climate Interactions,* P. V. Hobbs, Ed., Academic Press, 151–173.

Hess, M., and M. Wiegner, 1994: COP: A data library of optical properties of hexagonal ice crystals. *Appl. Opt.,* **33,** 7740–7746.

——, R. B. A. Koelemeijer, and P. Stammes, 1998: Scattering matrices of imperfect hexagonal ice crystals. *J. Quant. Spectrosc. Radiat. Transfer,* **60** (3), 301–308.

Heymsfield, A. J., 1993: Microphysical structures of stratiform and cirrus clouds. *Aerosol-Cloud-Climate Interactions,* P. V. Hobbs, Ed., Academic Press, 97–121.

Key, J. R., and J. M. Intrieri, 2000: Cloud particle phase determination with the AVHRR. *J. Appl. Meteor.,* **39,** 1797–1804.

King, M. D., 1993: Radiative properties of clouds. *Aerosol-Cloud-Climate Interactions,* P. V. Hobbs, Ed., Academic Press, 123–149.

Knap, W. H., M. Hess, P. Stammes, R. B. A. Koelemeijer, and P. D. Watts, 1999: Cirrus optical thickness and crystal size retrieval from ATSR-2 data using phase functions of imperfect hexagonal ice crystals. *J. Geophys. Res.,* **104,** 31 721–31 730.

Macke, A., J. Mueller, and E. Raschke, 1996: Single scattering properties of atmospheric ice crystals, *J. Atmos. Sci.,* **53,** 2813–2825.

Mishchenko, M. I., W. B. Rossow, A. Macke, and A. A. Lacis, 1996: Sensitivity of cirrus cloud albedo, bidirectional reflectance and optical thickness retrieval accuracy to ice particle shape. *J. Geophys. Res.,* **101,** 16 973–16 985.

Palmer, K. F., and D. Williams, 1974: Optical properties of water in the near-infrared. *J. Opt. Soc. Amer.,* **64,** 1107–1110.

Pilewskie, P., and S. Twomey, 1987a: Cloud phase discrimination by reflectance measurements near 1.6 and 2.2 μm. *J. Atmos. Sci.,* **44,** 3419–3421.

——, and ——, 1987b: Discrimination of ice from water in clouds by optical remote sensing. *Atmos. Res.,* **21,** 113–122.

Riedi, J., M. Doutriaux-Boucher, and P. Goloub, 2000: Global distribution of cloud top phase from POLDER/ADEOS I. *Geophys. Res. Lett.,* **27,** 1707–1710.

Rossow, W. B., and R. A. Schiffer, 1999: Advances in understanding clouds from ISCCP. *Bull. Amer. Meteor. Soc.,* **80,** 2261–2287.

Stammes, P., 1994: Errors in UV reflectivity and albedo calculations due to neglecting polarisation. *Proc. SPIE–Int. Soc. Opt. Eng.,* **2311,** 227–235.

Stephens, G. L., S.-C. Tsay, P. W. Stackhouse Jr., and P. J. Flatau, 1990: The relevance of the microphysical and radiative properties of cirrus clouds to climate and climate feedback. *J. Atmos. Sci.,* **47,** 1742–1753.

Stocker, T. F., and Coauthors, 2001: Physical climate processes and feedbacks. *IPCC WGI Third Assessment Report,* S. Manabe, and P. Mason, Eds., Cambridge University Press, 417–470.

Warren, S. G., 1984: Optical constants of ice from the ultraviolet to the microwave. *Appl. Opt.,* **23,** 1206–1225.

Wiscombe, W. J., and S. G. Warren, 1980: A model for the spectral albedo of snow. I: Pure snow. *J. Atmos. Sci.,* **37,** 2712–2733.